



Multifunctional tadpole-like bimetallic nanoparticles realizes synergistic sterilization with chemical kinetics and photothermal therapy

Yumeng Gao^{a,*}, Wentao Wang^{a,*}, Mohsen Mohammadniaei^b, Ming Zhang^{a,*}, Jian Shen^{a,*}, Ninglin Zhou^a

^a Jiangsu Collaborative Innovation Center for Biomedical Functional Materials, School of Chemistry and Materials Science, Nanjing Normal University, Nanjing 210023, PR China

^b Department of Health Technology, Technical University of Denmark, Kongens Lyngby 2800, Denmark

ARTICLE INFO

Keywords:

Tadpole-like nanoparticles
Photothermal
Peroxidase-like catalytic activity
Glutathione peroxidase-like activity
Catalase-like activity

ABSTRACT

Bacterial infection has become a global health issue. The misuse of antibiotics has been resulting in increased drug resistance and bioaccumulation. Therefore, developing a highly safe antibacterial agent, with high antibacterial performance is demanding. Inspired by the natural motors performing automated tasks in complicated living environments, we demonstrate tadpole-like nanoparticles (TNPs) with several functions, including high photothermal conversion efficiency, peroxidase-like catalytic activity, glutathione peroxidase-like activity, and catalase-like activity. TNPs produce hydroxyl radical ($\bullet\text{OH}$) at an extremely low concentration of hydrogen peroxide of 0.006%, which can damage bacterial cell membranes, proteins, and DNA. Moreover, the glutathione peroxidase-like activity disrupts the anti-oxidative mechanism of bacteria and improves the permeability of the cell membranes, consequently enhancing the killing effect of ROS. In addition, TNPs possess tadpole-like asymmetry to overcome Brownian motion, demonstrating strong directional motion propelled by O_2 . The *in vivo* experiments indicate that TNPs could also shorten the inflammatory period and promote angiogenesis, making them a very promising antibacterial agent.

1. Introduction

Currently, bacterial infections pose a substantial threat to people's quality of life and have contributed to increased mortality rates worldwide. However, misuse of antibiotics has caused drug resistance, faster bacterial evolution, and the pathogenesis of previously non-pathogenic microorganisms. Several superbugs have emerged around the world having multiple resistances to the majority of antibiotics [1–4]. In recent years, covalent organic framework derivatives [5–7], metal-organic frameworks [8–10], quaternary ammonium salts [11–13], etc., have been extensively researched as antibacterial agents, however, there are still unaddressed risks, such as being unfriendly to the environment. Therefore, it is very demanding to prepare and develop a highly efficient spatiotemporally controllable antibacterial agent, although, it requires an interdisciplinary approach.

Photothermal therapy (PTT) [14,15] and chemodynamic therapy (CDT) [16,17] have been widely employed in disease treatment, due to their non-invasiveness, low toxicity, and high specificity. In general, PTT

is a novel type of treatment that focuses on the target location and converts light energy into heat by irradiating an external light source using materials with high photothermal conversion efficiency. For example, Dong et al. [18] reported a novel multifunctional nanocapsule (PFP@PLGA/Cu₁₂Sb₄S₁₃)-mediated PTT alleviated hepatocellular carcinoma by inhibiting the RAS/MAPK/MT-CO₁ signaling pathway. Shan et al. [19] reported molecular engineering of therapeutic carrier-free co-delivery nanocomponents for self-sensitizing photothermal cancer treatment. Additionally, the polyvinyl alcohol/polyethylene glycol hydrogels loaded with photosensitizer methylene blue (MB) composite nanomaterials and biodegradable MoO_x nanoparticles (NPs) fabricated by Wang et al. [20] were used as 660 nm and NIR-II 1064 nm laser synergistic. The antibacterial efficacies of the light-activated wound dressings for photothermal-photodynamic therapy are 99.16% and 99.28% against *S. aureus* and *E. coli*, respectively. When the nanomaterial is exposed to the excitation light, three processes are triggered, including absorption, scattering, and reflection [21]. The PTT performance of the nanomaterial is determined not only by the light

* Corresponding authors.

E-mail addresses: wentwa@dtu.dk (W. Wang), mzhan@dtu.dk (M. Zhang), jshen@njnu.edu.cn (J. Shen).

<https://doi.org/10.1016/j.apcatb.2022.122314>

Received 29 September 2022; Received in revised form 29 November 2022; Accepted 18 December 2022

Available online 26 December 2022

0926-3373/© 2022 Elsevier B.V. All rights reserved.

absorption capacity but also by its photothermal conversion efficiency. The light source used for PTT is usually near-infrared light (NIR, 750–1350 nm) because of its low tissue absorption and scattering.

Most of the studies have focused on NIR-I (750–1000 nm), which still does not provide sufficient tissue penetration efficiency. However, NIR-II (1000–1700 nm) allows higher tissue exposure intensity, longer tissue exposure time, and deeper tissue penetration [22–24]. Moreover, biological tissues exhibit relatively lower light absorption at NIR-II due to the significant light scattering, which can remarkably avoid damage to normal tissues caused by long-term laser irradiation. In addition, PTT-related high temperature can alter the permeability of bacterial cell membranes, resulting in a disorganized bacterial cytoskeleton and impaired function. However, PTT-related high local temperature might destroy the surrounding healthy tissues, and the therapeutic efficacy might be weakened by the overactive immunogenicity. Therefore, it is an ideal development direction to combine PTT with other strategies to achieve a better synergistic therapy.

Bacteria can attach to implanted medical devices and lead to the formation of a biofilm, which has different microenvironments from normal tissues such as hypoxia, acidic environment, high GSH concentration, and overexpressed specific enzymes [25,26]. Recently, many therapeutic methods have been developed to resolve bacterial biofilm issues. For instance, transforming the high GSH microenvironment of biofilms by NO synergistically improves the photodynamic resistance to biofilms [27]. Or improving the hypoxic microenvironment of biofilms through the delivery of oxygen (O_2) and then treating them with antibiotics [28]. Therefore, altering the biofilm's hypoxia and the unique microenvironment with a high concentration of GSH is a feasible way to stand against bacterial infection.

Biofilms limit the accumulation of common antibacterial materials and greatly limit the action distance of ROS. Therefore, biomimetic nanomotors which can penetrate the biofilms and enter the deep tissues are particularly important. For example, the antibacterial nanomotors based on lysozyme developed by Kiristi et al. [29] can promote the interaction between enzymes and bacteria and prevent the aggregation of dead bacteria, thereby greatly enhancing the bactericidal ability. Peng et al. [30] prepared NO-driven nanomotors for bacterial biofilm elimination and endotoxin removal for the treatment of infected burn wounds with comprehensive anti-biofilm and anti-inflammatory effects.

Inspired by this, we developed multi-purpose nanozyme TNPs enabling simultaneous PTT, peroxidase-like catalytic activity, glutathione peroxidase-like activity, and catalase-like activity. ROS generated by TNPs can damage the cell membranes, proteins, and DNA of bacteria [31,32]. Concurrently, the high glutathione peroxidase-like activity neutralizes bacteria's antioxidant defense by disrupting their intracellular balance and making them sensitive to high O_2 levels, high permeability pressure, metal ions, etc. The fabricated TNPs with catalase-like activity can generate O_2 from an extremely low concentration of 0.006% hydrogen peroxide, thus the space asymmetry directs the TNPs to penetrate deep tissues. Altogether, the developed TNPs are capable of increasing the permeability of bacteria membranes which can enhance the killing range of ROS and achieve the purpose of synergistic sterilization.

2. Experimental section

2.1. Materials

Copper chloride dihydrate ($CuCl_2 \cdot 2 H_2O$, 99.0%) was purchased from Shanghai Xinbao Fine Chemical Factory; polyvinylpyrrolidone (PVP, GR, K30), glucose (AR), L(+)-ascorbic acid (AR, $\geq 99.7\%$), Ethylene Glycol (AR, $\geq 99.5\%$), Sodium Chloride (NaCl, AR, $\geq 99.5\%$), 30% Hydrogen Peroxide (AR), Acetic Acid (AR, $\geq 99.5\%$), and Dimethyl Sulfoxide (AR, $\geq 99.5\%$) were purchased from Sinopharm Group Chemical Reagent Co., Ltd.; polyethylene glycol 4000 (PEG₄₀₀₀, CP) was from Xilong Science Co., Ltd.; sodium molybdenum oxide dihydrate

(AR, 99.0%) and lauric acid (AR, 98%) were obtained from Shanghai Macklin Biochemical Co., Ltd.; thioacetamide (AR, $\geq 99\%$) was obtained from China Sinopharm Shanghai Chemical Reagent Company; ethanol (AR, $\geq 99.7\%$) were purchased from Wuxi Yasheng Chemical Co., Ltd.; phospholipid polyethylene glycol carboxyl group (DSPE-PEG₂₀₀₀-COOH) was purchased from Pengshuo Biology; Calcein-AM/PI live cell/dead cell double staining kit, tryptone (BR), and MTT were obtained from Solarbio; 3,3',5,5'-tetramethylbenzidine (TMB, 98%), 2,7-dichloro-fluorescein dihydrogen Diacetate (DCFH-DA, $\geq 97\%$), o-phenylenediamine (OPDA, AR, 98%), chloroacetaldehyde, hydrated (AR, 99%) and propidium iodide (94%) were purchased from Aladdin Chemical Reagent Co., Ltd.; 5,5'-Dithiobis(2-nitrobenzoic acid) (DTNB, 98%) was purchased from Bide Pharmaceuticals; anhydrous sodium acetate ($\geq 98.5\%$) was purchased from Shanghai Shisihewei Chemical Co., Ltd. All chemicals were used directly without further purification.

Mouse fibroblast cells (L929), phosphate-buffered saline (PBS, pH 7.4), Dulbecco's modified eagle medium (DMEM), and fetal bovine serum (FBS) were purchased from Jiangsu KeyGEN Bio-Tech Corp., Ltd. All studies were conducted according to the institutional guidelines of Nanjing Normal University.

2.2. Synthesis of Cu_2O

In 100 mL deionized water, 0.171 g $CuCl_2 \cdot 2 H_2O$ and 3.333 g PVP were dissolved and magnetically stirred for 10 min. Then the NaOH solution (2 M, 10 mL) and ascorbic acid aqueous solution (0.6 M 10 mL) were prepared and mixed under magnetic stirring. After 1 h, the products were recovered by centrifugation at 10,000 rpm for 5 min and washed three times with deionized water and ethanol, and the samples were placed in an oven and dried at 60 °C [33].

2.3. Synthesis of Cu_2MoS_4 @PEG

40 mg of the above Cu_2O powder and 120 mg of glucose were dissolved in 20 mL of ethylene glycol by ultrasonication; another 70 mg of $Na_2MoO_4 \cdot 2 H_2O$ and 120 mg of thioacetamide were dissolved in the above solution and ultrasonicated for 30 min. The mixed solution was transferred to a 45 mL polytetrafluoroethylene reactor and reacted at 200 °C for 24 h. The solids were isolated by centrifugation at 10,000 rpm and washed three times with deionized water and ethanol, respectively. The prepared Cu_2MoS_4 was dissolved in 50 mL of deionized water, 5 mg of PEG-4000 was added to the solution, and the PEGylated Cu_2MoS_4 was collected by centrifugation after magnetic stirring for 1 h, washed several times with deionized water, and then placed in an oven and dried at 60 °C.

2.4. Synthesis of Cu_2MoS_4 @PEG@DSPE (TNPs)

10 mg of the above Cu_2MoS_4 @PEG was dissolved in 10 mL of absolute ethanol by ultrasonication. Then add 5 mg of DSPE-PEG-COOH, and stir magnetically for 6 h; add 1 mL of 20 mg/mL tetraethylthiuram disulfide, continue to stir for 24 h, centrifuge at 10,000 rpm, wash three times with absolute ethanol, then re-add 10 mL of absolute ethanol and 10 mg of lauric acid, stir for 6 h, centrifuge at 10,000 rpm, and washed with absolute ethanol 3 times, and finally placed in an oven and dried at 60 °C.

2.5. Characterization and methods

This part is in the [supplementary materials](#).

3. Results and discussion

3.1. Characterization of TNPs

Nanozymes based on the catalytic reaction of multivalent metal ions,

which mimicked the functions of natural enzymes had shown a prominent effect in bacteriostasis [34,35]. Transition metal chalcogenides, such as copper-molybdenum sulfide (Cu_2MoS_4) have received special attention due to their excellent catalytic performance. The hollow mesoporous Cu_2MoS_4 NPs with a great cavity (Fig. 1) were synthesized by using Cu_2O nanospheres as self-sacrificial [33] and then modified to improve their biocompatibility. The schematic diagram of the synthesis of TNPs is shown in Fig. 1. The added glucose coats the surface of Cu_2O , followed by forming a glucose-derived carbon protective layer as previously reported [33]. In Fig. 2A, transmission electron microscopy (TEM) shows that Cu_2MoS_4 NPs are consistent with the previous report [33,34]. It is a hollow mesoporous sphere with a uniform shape and size. The modified TNPs (Fig. 2B) represent tadpole-like structures with uniform shape and size distribution. The TNPs showed a smaller size with uniform distribution (ca. 300 nm). The high-resolution TEM (HR-TEM) image (Fig. 2C, S1) shows a clear lattice spacing of 0.27 nm, belonging to the (020) plane of the Cu_2MoS_4 NPs [33]. As shown in Fig. 2D and S2, the distribution of the elements Cu, C, and P on the TNPs can be seen.

The surface elemental compositions of TNPs were analyzed by X-ray photoelectron spectroscopy (XPS). As displayed in Fig. 2E, S, Mo, C, N, O, and Cu elements can be observed from the XPS wide-scan spectra of TNPs, and the compositions are S 18.63%, Mo 6.02%, C 39.6%, N 9.58%, O 11.53%, and Cu 14.64%, respectively. Fig. 2F-H show that Cu is composed of valence states of Cu^+ (931.8 eV) and Cu^{2+} (933.2, 953.0 eV), while Mo presents in the valence state of Mo^{4+} (229.8 eV) and Mo^{6+} (232.8 eV) [33,34]. Moreover, the binding energy of 161.5 and 162.6 eV belong to S 2p_{3/2} and S 2p_{1/2}, respectively (Fig. 2H), indicating that the valence state of Cu, Mo, and S in TNPs is +1, +6, and -2. The existence of $\text{Cu}^+/\text{Cu}^{2+}$ and $\text{Mo}^{4+}/\text{Mo}^{6+}$ redox pairs furnish enormous potential for catalase-like and glutathione oxidase-like activities of TNPs. Fourier transform infrared spectroscopy (FT-IR) of TNPs shows the stretching vibration of CH_2 at 2922 cm^{-1} , the stretching vibration of $\text{C}=\text{O}$ at 1629 cm^{-1} , the bending vibration of $\text{C}-\text{H}$ at 1384 cm^{-1} , and $\text{C}-\text{N}$ vibrations at 1461 cm^{-1} , which indicate that the

NPs have been successfully modified (Fig. 2I). Distinct diffraction rings can be seen in the selected area electron diffraction pattern of the TNPs (Fig. S3). X-ray powder diffraction (XRD) in Fig. S4 demonstrates that the diffraction peaks of TNPs are located at 17.58°, 18.54°, 29.27°, 37.61°, 47.38°, and 49.36°, respectively, belonging to I- Cu_2MoS_4 NPs (body-centered space group I-42 m) (002), (101), (112), (202), (220), and (204) planes, consistent with the results of SAED.

The subsequent introduction of PEG₄₀₀₀ and DSPE-PEG₂₀₀₀-COOH, combined with Cu_2MoS_4 through non-covalent interaction, improves the biocompatibility of NPs. The zeta potential of TNPs changes from -10.75 mV to -25.2 mV after modification (Fig. S5). The Raman peaks (Fig. 2J) at 197.9 cm^{-1} and 260.4 cm^{-1} can be assigned to B_2 and B_1 , respectively, which is consistent with the existing literature [36–39]. The Brunauer-Emmett-Teller (BET) measurements in Fig. 2K show that the TNPs have a large surface area (84.5998 m^2/g), and the pore size distribution is shown in Fig. 2L. A large number of pores with a size of 8.07 nm facilitates efficient subsequent exposure to active sites. The above characterizations prove that the head and tail of TNPs are all composed of Cu_2MoS_4 . We speculate that the formation of tadpole shapes is due to the irregular expansion of hollow spherical shell shapes in adverse environments.

3.2. Photothermal property of TNPs

A remarkable photothermal agent is anticipated to possess intense absorbance in the NIR area, which is the lucency window for PTT agents shown in Fig. 3A, TNPs exhibit notable optical absorption in the NIR region, indicating that TNPs possess a superior photothermal effect. Further deionized water was used as a negative control to study the photothermal effect of TNPs under irradiation at 1064 nm. For the control group, no obvious temperature change was observed, the temperature rose to 36.5 °C after 10 min of irradiation, while the TNPs aqueous solution of 250 $\mu\text{g}/\text{mL}$ was heated to 60.4 °C within 10 min. TNPs show elevated temperature with the increase in irradiation time, concentration, and irradiation power density (Figs. 3B, 3C). The

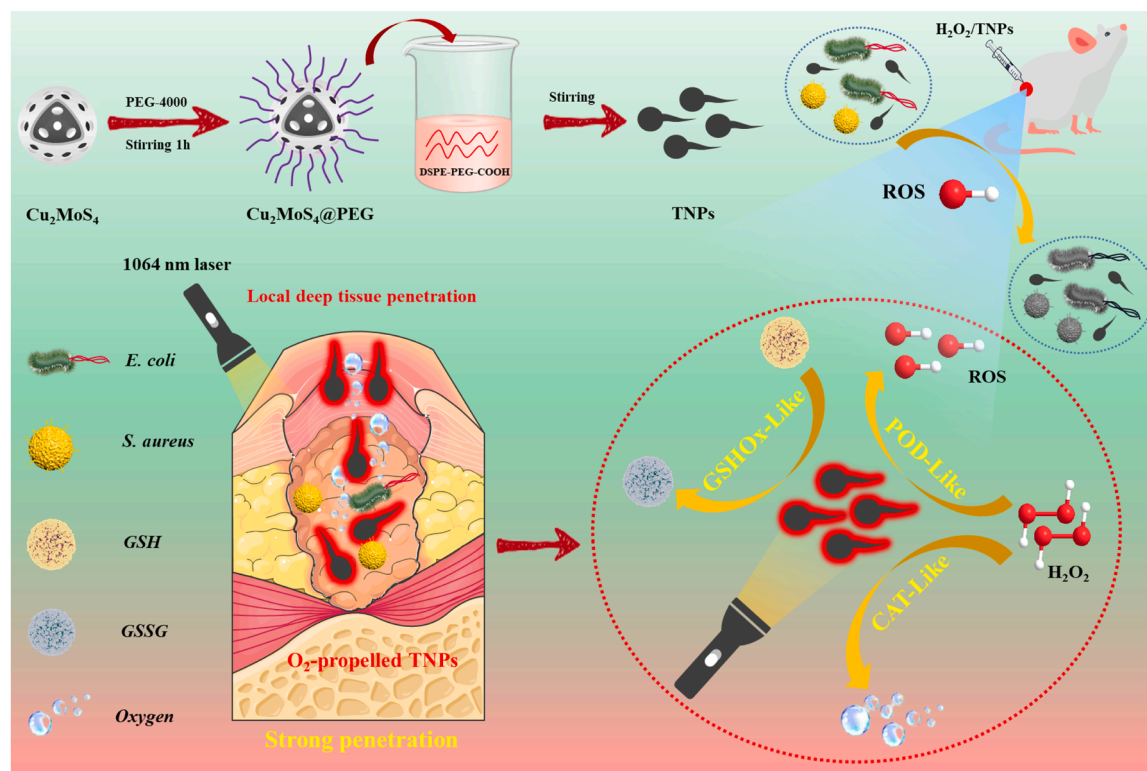


Fig. 1. Schematic diagram and mechanism of preparation of tadpole-like NPs for synergistic antibacterial.

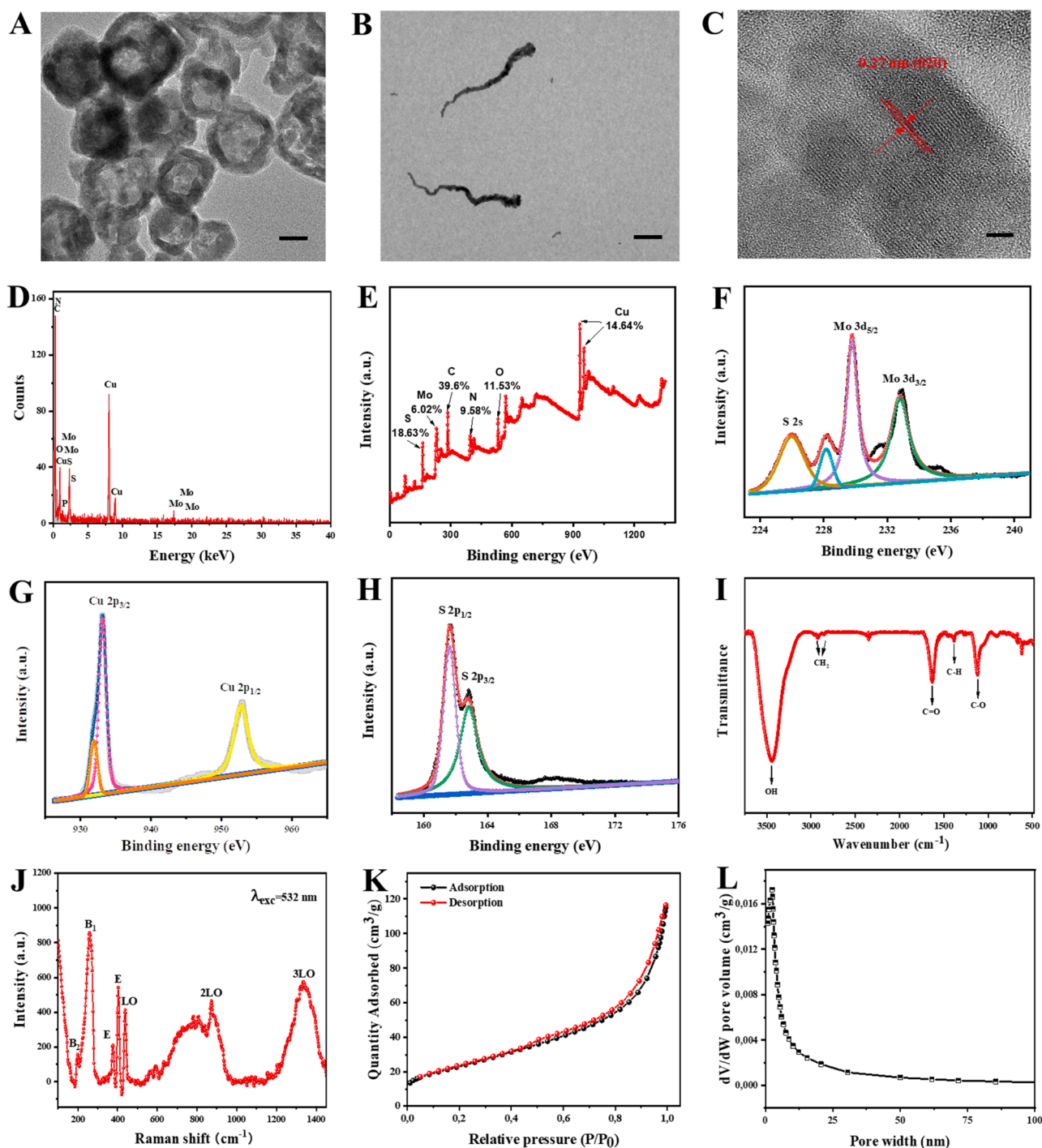


Fig. 2. A) TEM image of Cu_2MoS_4 NPs. Scale bar= 80 nm. B) TEM image of TNPs. Scale bar= 50 nm. C) HRTEM image of TNPs. Scale bar= 5 nm. D) EDS image of TNPs. E-H) XPS high-resolution scans of TNPs, Mo 3d, Cu 2p, and S 2p. (I) FTIR spectra of TNPs. J) Raman spectra of TNPs. K) N_2 -isotherms of TNPs. L) Pore-size distribution of TNPs.

photothermal conversion efficiency is calculated to be 39.59% (Figs. 3E, 3F), much higher than that for other reported PTT agents in NIR-II 1064 nm. In addition, as shown in Fig. 3D, when the TNPs were irradiated with the “ON/OFF” laser 5 consecutive times, the temperature increase amplitude of the TNPs did not decrease significantly, indicating the good photothermal stability of the TNPs. Thereby, TNPs can be regarded as ideal candidates in the field of phototherapy.

3.3. O_2 generation and motion behavior of TNPs

In recent years, catalytic therapy has received increasing attention in antimicrobial treatments. TNPs of different concentrations (0, 50, 100, 150, 200, and 250 $\mu\text{g}/\text{mL}$) were co-incubated with hydrogen peroxide (1 M) for 4 h. Fig. 3G shows that after 1 h of catalysis, a small number of bubbles have been generated in groups with concentrations of 100, 150, 200, and 250 $\mu\text{g}/\text{mL}$. With the concentration of TNPs and the time increased, the number of bubbles increased. In addition, we measured the concentration of O_2 in the solution within 4 h. As shown in Fig. S6,

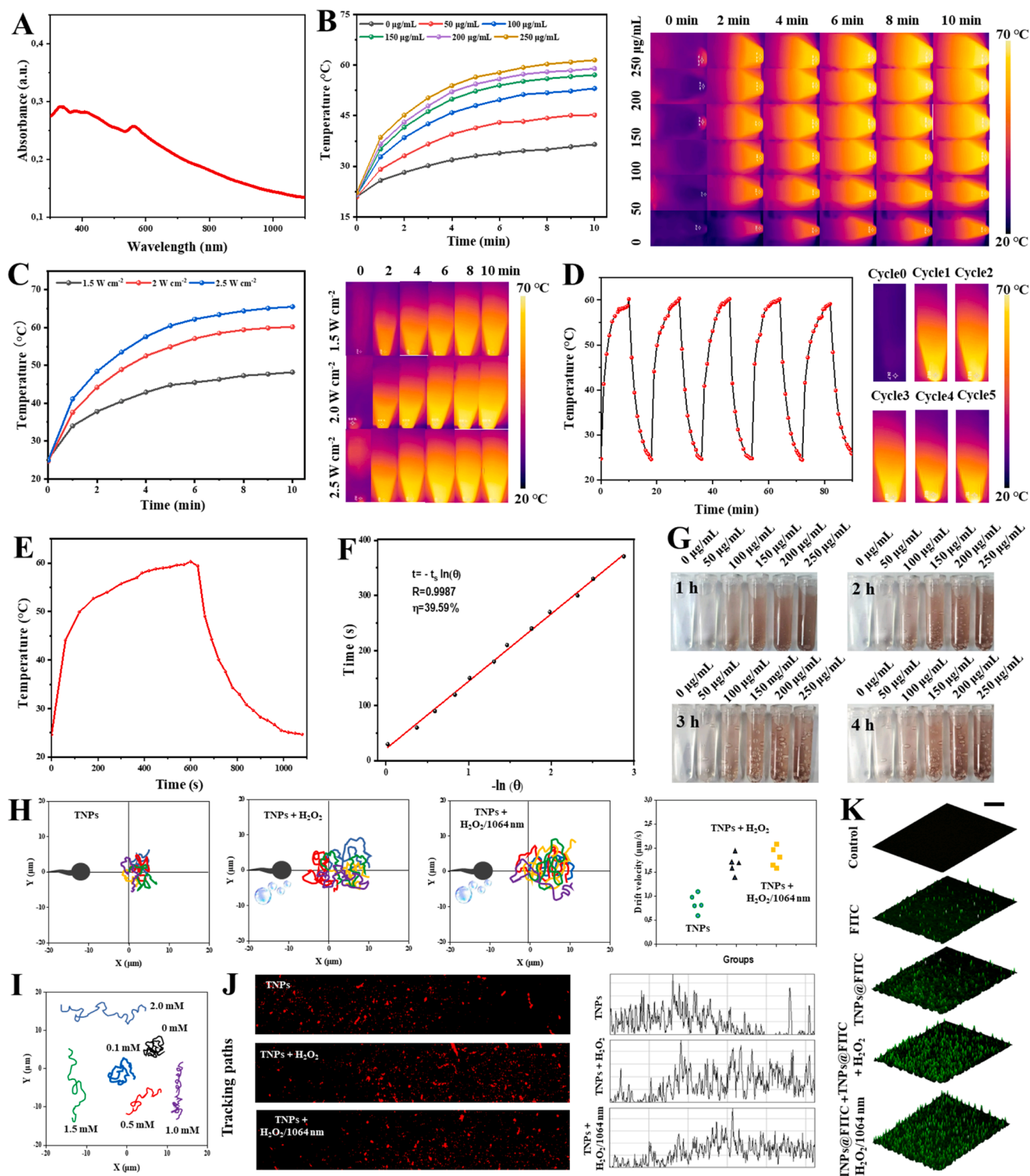


Fig. 3. A) UV-Vis-NIR absorption spectra of TNPs. B) Photothermal heating curves and thermal images of TNPs solutions at varied concentrations. C) Temperature change and thermal images of TNPs with NIR-II light irradiation (1.5, 2.0, and 2.5 W/cm²). D) Repeated heating/cooling curves and thermal images of TNPs aqueous dispersion (250 µg/mL) under 1064 nm irradiation (2.0 W/cm²). E) Temperature profiles of TNPs (250 µg/mL) dispersed in water irradiated by 1064 nm (2.0 W/cm²) followed by natural cooling after the light is turned off. F) Measurement of the time constant of the heat transfer from the system using linear regression of the cooling profile. G) Plot of the number of O₂ bubbles generated by H₂O₂ after incubation with different concentrations of TNPs. H) The trajectory and speed of TNPs under H₂O₂ and 1064 nm. I) The trajectory of TNPs under H₂O₂ (0, 0.1, 0.5, 1.0, 1.5, and 2.0 mM) and NIR-II light irradiation (1064 nm, 2.0 W/cm²). J) Tracking paths and signal diagrams of pure TNPs, TNPs+H₂O₂, and TNPs+H₂O₂/1064 nm. K) Images of the uptake ability of *S. aureus* for pure TNPs, TNPs+H₂O₂, and TNPs+H₂O₂/1064 nm, Scale bar = 20 µm, * $P < 0.05$.

there was no obvious O_2 production in the pure TNPs group and the H_2O_2 group, while the O_2 concentration in the TNPs+ H_2O_2 group increased with time. The O_2 concentration reached 1.6 mg/mL after 4 h. This is attributed to the presence of Cu^+/Cu^{2+} and Mo^{4+}/Mo^{6+} redox

pairs, in which H_2O_2 is oxidized to produce O_2 in the presence of Cu^{2+} and Mo^{6+} , demonstrating the excellent catalase-like activity of TNPs.

To evaluate the mobility of TNPs driven by O_2 , we recorded the motion trajectories within 25 s by optical tracking. As shown in Fig. 3H,

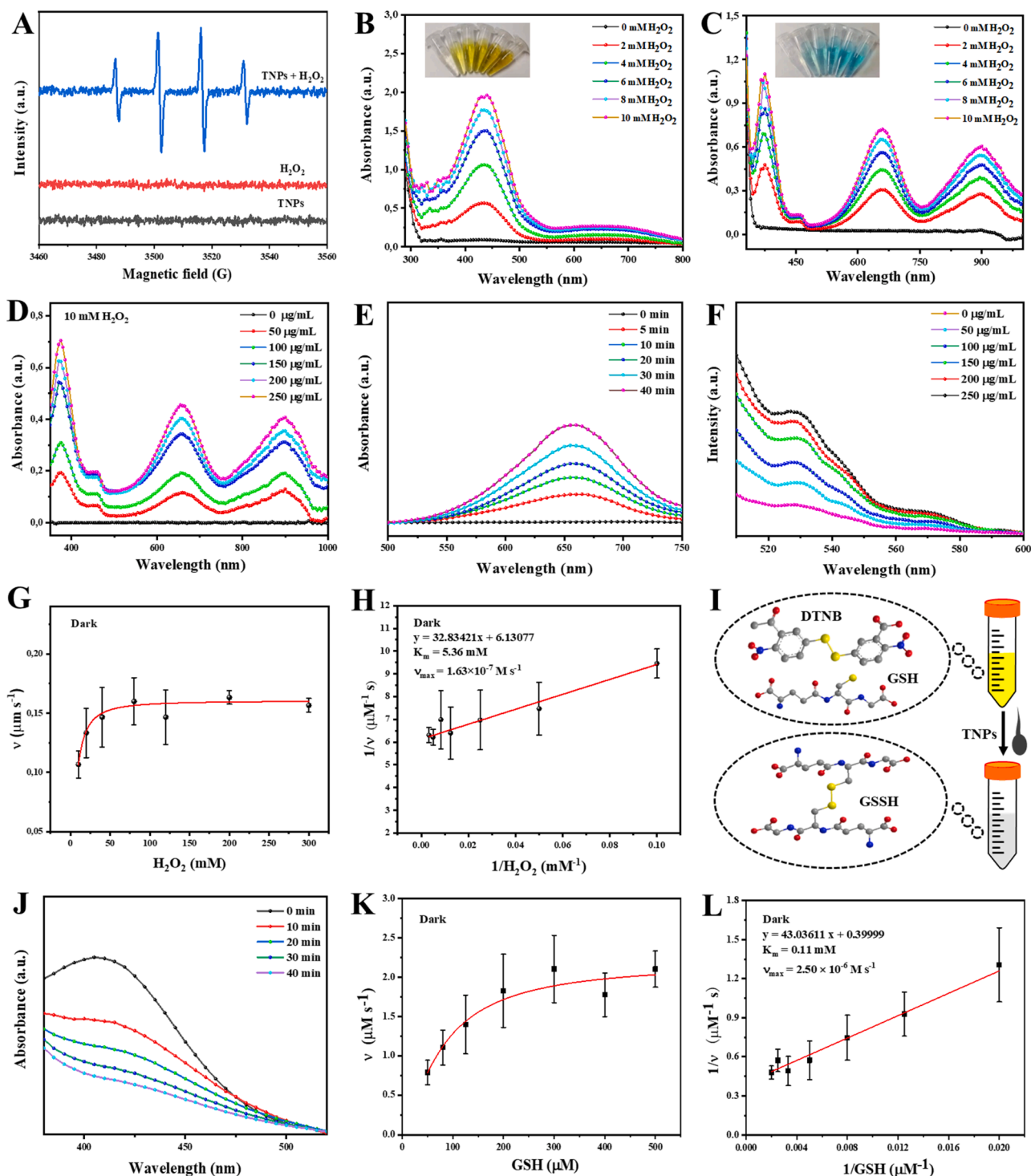


Fig. 4. A) ESR spectra of TNPs+ H_2O_2 , TNPs, and H_2O_2 for detection of $\bullet OH$ radicals. B) Peroxidase-like activity of TNPs (250 $\mu g/mL$) at different substrate concentrations using OPDA (1 mg/mL) as an indicator. The inset shows the color change of OPDA under different experimental conditions. C) Peroxidase-like activity of TNPs (250 $\mu g/mL$) at different substrate concentrations using TMB as an indicator. The inset shows the color change of TMB under different experimental conditions. D) Concentration-dependent absorption changes of TMB in the presence of TNPs (0, 50, 100, 150, 200, and 250 $\mu g/mL$) and H_2O_2 (10 mM). E) Time-dependent absorption changes of TMB in the presence of TNPs (250 $\mu g/mL$) and H_2O_2 (10 mM). F) Concentration-dependent intensity changes of DCFH-DA in the presence of TNPs (0, 50, 100, 150, 200, and 250 $\mu g/mL$) and H_2O_2 (10 mM). G) Michaelis-Menten kinetic analysis and H) Lineweaver-Burk plotting for TNPs with H_2O_2 as a substrate. I) Schematic diagram of the mechanism of using DTNB as a GSH probe. J) GSH consumption after being treated with TNPs. K) Michaelis-Menten kinetic analysis and L) Lineweaver-Burk plotting for TNPs with GSH as a substrate.

the motion range of the pure TNPs group was within 7 μm . After applying H_2O_2 and 1064 nm laser irradiation, the motion range of TNPs expanded to 16 μm , reaching 53 times the length of TNPs themselves, showing enhanced Brownian motion [40–42], and the movement speed increased from 0.8 $\mu\text{m/s}$ to 1.6 $\mu\text{m/s}$ and 1.8 $\mu\text{m/s}$. In order to observe the motion state of TNPs more directly, we used an inverted fluorescence microscope to record the movement images of TNPs at different times. As can be seen from Fig. S7, TNPs showed slight Brownian motion in situ without any treatment. However, when hydrogen peroxide was added, TNPs showed obvious directional motion, which became more intense under the condition of 1064 nm. Moreover, as can be seen from Fig. 3I, when the concentration of H_2O_2 is insufficient (0 mM, 0.1 mM), only the pure Brownian motion in situ is observed; while as the concentration of H_2O_2 increases, the path of the TNPs becomes directional advancing. This peculiar motion may be due to the persistent immobilization of the O_2 bubbles and the asymmetric tadpole shape, which not only accelerated the motion but also propelled the TNPs forward.

Next, rat tail collagen was gently mixed with aqueous sodium hydroxide solution and EDTA-2Na aqueous solution [42], then added to the micro slide capillary. After overnight incubation at 37 $^\circ\text{C}$, the TNPs mixed with H_2O_2 were added from the left end of the capillary (the working concentrations of TNPs and H_2O_2 were 250 $\mu\text{g/mL}$ and 2 mM, respectively). After 40 min, the moving distance of TNPs in the micro glass tube was observed under a laser confocal microscope (LSCM). In the *in vivo* pustule model, the dense interstitial extracellular matrix (ECM) and bacterial biofilm hinder the deep penetration of nanomedicines and greatly limit the scope of ROS action. As shown in Fig. 3J, we examined whether TNPs fueled by H_2O_2 could exhibit better ECM penetration ability, and the results showed that the TNPs in the TNPs+ H_2O_2 group and the TNPs+ H_2O_2 /1064 nm group almost all moved to the right end of the capillary, while the pure TNPs group showed random dispersion, and only a few nanoparticles appeared on the right end, which indicated that the penetration behavior of TNPs was faster and deeper after obtaining self-propelled force. In addition, TNPs were labeled with fluorescein isothiocyanate (FITC) to observe the uptake of TNPs by *S. aureus* under different conditions. As shown in Fig. 3K and Fig. S8, with the addition of H_2O_2 , the fluorescence was significantly enhanced, showing enhanced uptake of TNPs. Taken together, as shown in Fig. S11, the self-propulsion of O_2 enables TNPs to exhibit enhanced directional movement and overcome the obstacles of the ECM and bacterial cell membranes, resulting in a greatly enhanced antibacterial effect, which lays the foundation for the treatment of deep tissue infections.

3.4. Determination of ROS

The peroxidase-like activity of TNPs was investigated by the electron spin resonance (ESR) method. As shown in Fig. 4A, TNPs can successfully catalyze the formation of $\bullet\text{OH}$ from H_2O_2 and catalyze 5-tert-butoxycarbonyl-5-pyrroline-N-oxide (BMPO) to form $\bullet\text{OH}/\text{BMPO}$ with a characteristic signal peak of 1:2:2:1 [43]. Then the POD and GSHOx-mimic enzyme activities of TNPs were examined at room temperature. The POD-mimic activity of TNPs was examined by a colorimetric reaction based on o-phenylenediamine (OPDA) and 3,3',5,5'-tetramethylbenzidine (TMB). In the presence of H_2O_2 , the $\bullet\text{OH}$ generated from the POD-like activity of TNPs could catalyze the oxidation of OPDA to yellow-colored oxidized OPDA (DAPN) and the oxidation of TMB to oxTMB of blue-colored. As shown in Figs. 4B and 4C, the increasing absorption peaks of DAPN and oxTMB with the concentration of H_2O_2 were observed when TNPs were added to the mixture, indicating that TNPs catalyzed H_2O_2 to generate more $\bullet\text{OH}$. In addition, the POD-like activity also shows concentration dependence on TNPs and time dependence (Figs. 4D, 4E). The colorimetric TMB reaction followed a typical Michaelis-Menten kinetics with a Michaelis-Menten constant (K_m) and a maximal reaction velocity (V_{max}) of 5.36 mM and $1.63 \times 10^{-7} \text{ M s}^{-1}$, respectively (Figs. 4G, 4H). In order to explore the influence of the photothermal effect on peroxidase-like

activity in TNPs, the Michaelis-Menten kinetic analysis for TNPs with H_2O_2 was investigated under a 1064 nm laser. Under the irradiation of 1064 nm, the catalytic rate of hydrogen peroxide was increased significantly, indicating that the photothermal effect can effectively improve the peroxidase-like activity, so as to achieve a synergistic antibacterial effect (Fig. S9). Additionally, as a commonly used oxidative stress reagent, DCFH-DA is often used as a probe to detect ROS. After being oxidized by ROS, DCFH will generate a strong fluorescent product DCF. As shown in Fig. 4F, the enhanced fluorescence peak of DCF with the concentration of TNPs was observed, which indicated that the production of ROS was concentration-dependence.

The accumulation of intracellular reactive oxygen species due to respiration or environmental factors can cause damage to bacterial proteins, cell membranes, lipids, and DNA. To avoid this, bacteria have developed their own anti-oxidative systems during evolution. Glutathione plays an important role in the antioxidative mechanism of bacteria, they can participate in the redox reactions in metabolism, maintain bacterial intracellular balance through enzymatic reactions, and protect bacteria from high O_2 levels, high osmotic pressure, metal ions, etc. Cu^{2+} and Mo^{6+} in TNPs can oxidize GSH to generate GSSG to disrupt the antioxidant defense mechanism of bacteria, thereby assisting PTT and CDT. The amount of remaining GSH was determined using 5,5'-dithiobis (2-nitrobenzoic acid) (DTNB) as a probe [44]. DTNB and GSH would generate TNB with a typical absorbance peak at 412 nm (Fig. 4I). As shown in Fig. 4J, the absorbance of GSH at 412 nm gradually decreased with time, and the Michaelis-Menten kinetics (Figs. 4K, 4L) was calculated as $K_m = 0.11 \text{ mM}$, $V_{\text{max}} = 2.50 \times 10^{-6} \text{ M s}^{-1}$. Similarly, the glutathione peroxidase-like activity was also significantly enhanced under photothermal conditions (Fig. S10).

3.5. In vitro antibacterial assays

To further verify the antibacterial mechanism, the variability of ROS in *E. coli* and *S. aureus* was analyzed by recording the fluorescence intensity using a probe of DCFH-DA. As shown in Fig. 5A, the experiments were divided into 6 groups: (1) Control; (2) H_2O_2 ; (3) TNPs; (4) TNPs+ 1064 nm; (5) TNPs+ H_2O_2 ; and (6) TNPs+ H_2O_2 /1064 nm. After co-incubating for 4 h, both the TNPs+ H_2O_2 group and the TNPs+ H_2O_2 /1064 nm group exhibited bright green fluorescence, suggesting that TNPs with excellent POD-like activity could induce overproduction of ROS, thus resulting in the damage of the antioxidant defense system.

Following the multifunctional nature of TNPs, their antimicrobial efficacy was investigated *in vitro*. Two representative pathogenic bacteria, *S. aureus* and *E. coli*, were chosen as experimental modal strains. The antibacterial ability of TNPs *in vitro* assisted by H_2O_2 and NIR light was first explored by the plate counting method. As shown in Fig. 5B–5E, the experiments were divided into 4 groups: (1) TNPs; (2) TNPs+ H_2O_2 ; (3) TNPs+ 1064 nm; and (4) TNPs+ H_2O_2 /1064 nm. The working concentration of H_2O_2 in the experiment was 2 mM, and the irradiation time of the 1064 nm laser (2.0 W/cm^2) was 10 min. In group (1), with the increase in sample concentration, the bacterial numbers of *S. aureus* and *E. coli* did not decrease significantly, and the final bacterial survival rates were 81% and 83%, respectively, which indicated that the bactericidal effect of the sample was feeble. In groups (2) and (3), the antibacterial group after a single method showed a more obvious bactericidal effect, in which the bactericidal rates of the two bacteria were increased to 52% and 65% after the addition of H_2O_2 . While after the application of 1064 nm, the bactericidal rates of the two bacteria were increased to 72% and 70%, respectively. However, the synergistic group was the best group with the final bactericidal rates of 99.2% and 92.8%.

To assess the cytotoxicity of TNPs, further membrane integrity imaging experiments were performed using propidium iodide (PI) dye (Fig. 5F). Visual inspection of the red fluorescence signal revealed a critical breakdown of membrane integrity in *E. coli* and *S. aureus* in the synergistic group. In contrast, the red fluorescent signal was found to be lower in bacteria treated with CDT or PTT. In summary, the penetrating

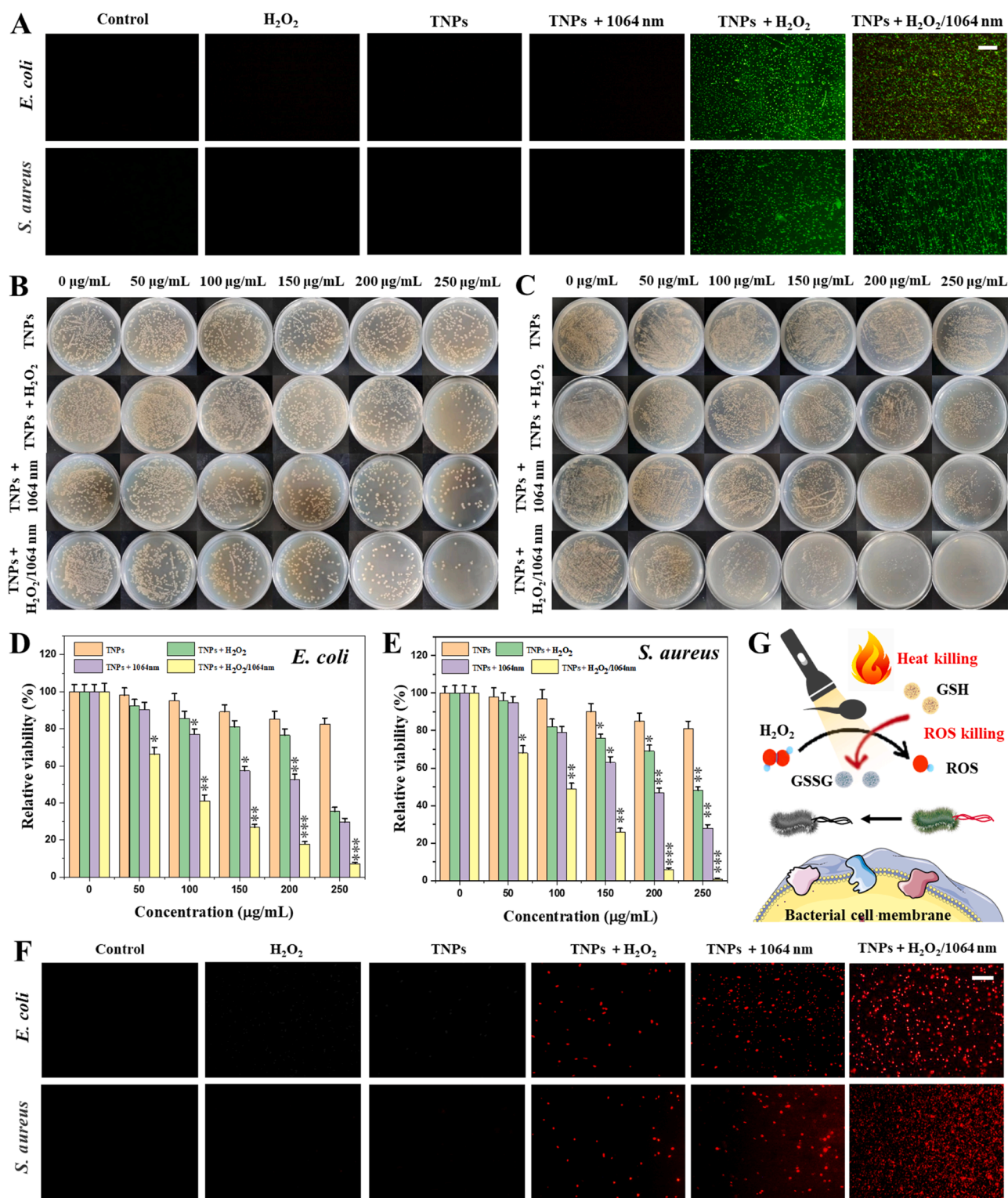


Fig. 5. A) Fluorescence images of ROS production in bacteria using DCFH-DA (40 μM) as a fluorescent probe for ROS. B) Colonies of *E. coli* and C) *S. aureus* after different treatments. D) Survival rates of *E. coli* and E) *S. aureus* after treatment with TNPs, TNPs+ H_2O_2 , TNPs+ 1064 nm, and TNPs+ H_2O_2 /1064 nm. (* $P < 0.5$, ** $P < 0.01$, and *** $P < 0.001$ compared with control group). F) Fluorescence staining images of *E. coli* and *S. aureus* using PI after different treatments. Scale bar= 10 μm . G) Antibacterial mechanism of TNPs.

dye PI was detected in bacteria cells in both the single-method and synergistic antibacterial groups, while the synergistic group tended to cause the greatest damage. There are two main reasons for the excellent bactericidal ability of the synergistic group (Fig. 5G): first, the long tails of TNPs can combine with the bacterial cell membrane, thereby causing

the cell membrane to loosen, resulting in leakage of bacterial contents and even apoptosis; second, 1064 nm light forms a local high temperature, which can promote the ablation of bacterial cell membranes and accelerate the catalytic reaction, which has a synergistic sterilization effect.

To evaluate the interaction between TNPs and bacteria, the cell membrane integrity of bacteria treated with TNPs was observed by TEM and SEM. The experiments were carried out in 6 groups: (1) Control; (2) H_2O_2 ; (3) TNPs; (4) TNPs+ H_2O_2 ; (5) TNPs+ 1064 nm; and (6) TNPs+ H_2O_2 /1064 nm. TEM analysis [45] of *E. coli* and *S. aureus* showed that TNPs were tightly adsorbed around the bacteria and even entered

the bacterial cells (Fig. 6A). At the same time, unlike the untreated rod-shaped bacteria, the morphology of *E. coli* is broken and uneven, and obvious leakage of the contents can be seen; *S. aureus* is also different from the normal smooth spherical shape, its cell membrane shows ablated and broken state. Secondly, as shown in Fig. 6B, the bacteria in the control group had intact morphology and smooth cell membranes, while

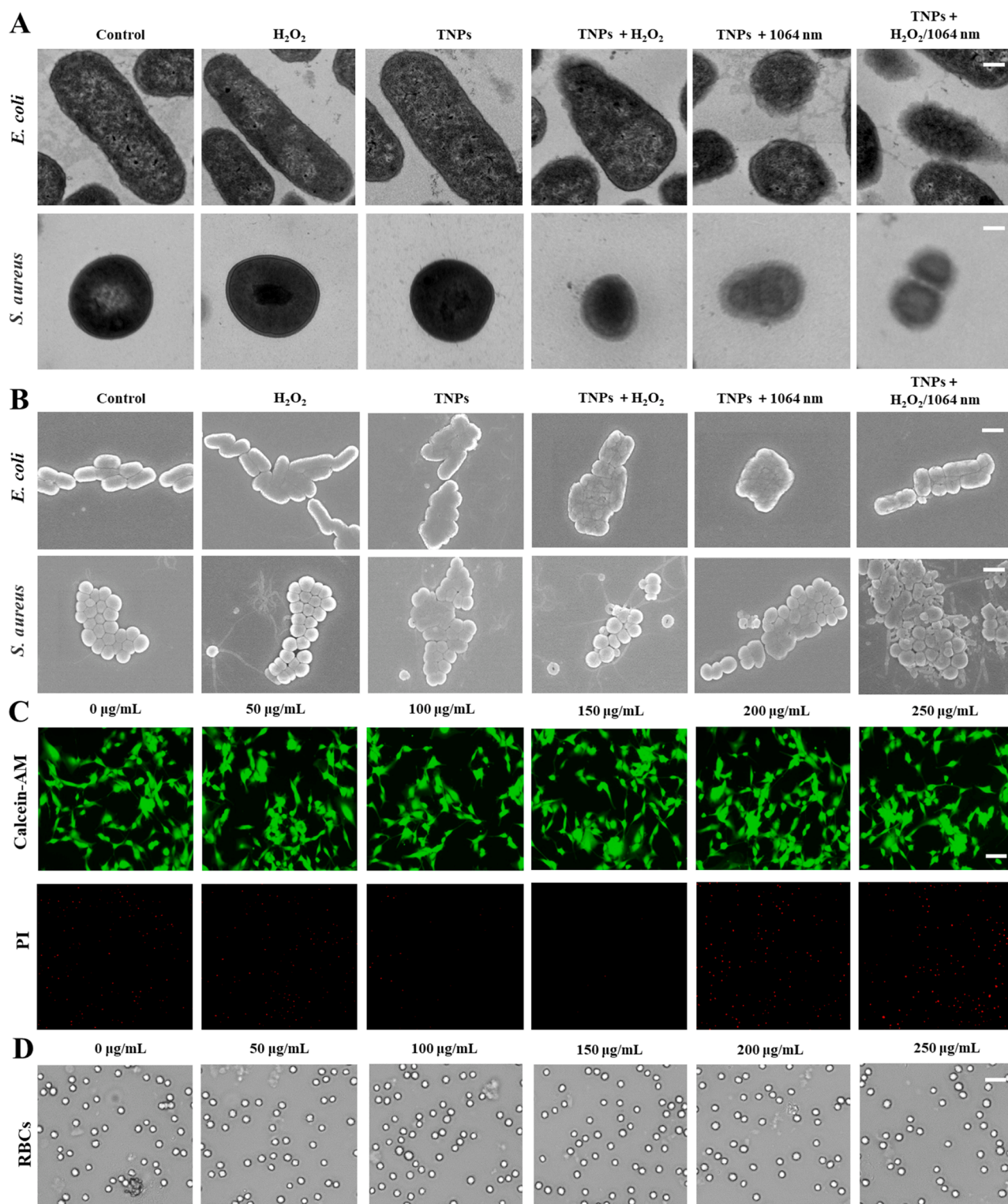


Fig. 6. A) TEM (Scale bar = 0.1 μm) and B) SEM (Scale bar = 0.1 μm) images of *E. coli* and *S. aureus* with different treatments. C) Live/Dead staining images of L929 cells after treated with TNPs (0, 50, 100, 150, 200, and 250 $\mu g/mL$). Scale bar = 30 μm D) The optical images of RBCs after treated with TNPs (0, 50, 100, 150, 200, and 250 $\mu g/mL$). Scale bar = 30 μm .

the bacterial cell membranes in groups (4) and (5) treated with a single antibacterial treatment showed slight shrinkage and cracks. About 50% of the bacterial membranes of *E. coli* and *S. aureus* were destroyed. However, the destruction of bacterial cell membranes by the synergistic group was the most obvious, resulting in the leakage of bacterial contents, which further supports the importance of synergistic antibacterial. These results confirm that TNPs may cause damage to the whole plasma membrane.

3.6. In vitro biocompatibility

To evaluate the biocompatibility and cytotoxicity of TNPs, we first measured the cell viability after treatment with different concentrations of TNPs by a standard 3-(4,5-Dimethylthiazol-2-yl)-2,5-diphenyltetrazolium bromide (MTT) assay [46]. As shown in Fig. S12, after 4 h of co-culture, the viability of L929 cells did not decrease significantly, and the cell viability remained at 84.42% after being treated with 250 $\mu\text{g/mL}$ TNPs. To better visualize the cytotoxicity of TNPs using fluorescence microscopy, L929 cells were stained with Calcein-AM and PI dyes. Apoptotic cells were stained red by PI, and the live cells were stained green by Calcein-AM. The staining results of live and dead cells were consistent with the results of the MTT test. As shown in Fig. 6C, after being treated with 250 $\mu\text{g/mL}$ TNPs, only a few cells showed weak red fluorescence, indicating that the cells had a very small amount of apoptosis, but no obvious modification occurred. These results indicated that TNPs have great potential as a low-toxicity antibacterial agent. Moreover, the hemolytic activity of TNPs at different concentrations was detected, with PBS as the control group (Fig. 6D). Hemolysis refers to the interaction and incompatibility of the sample with red blood cells (RBCs), and the sample is considered safe when its hemolysis rate is less than 5% [47]. Fig. S13 shows that the hemolysis rate of TNPs at a concentration of 250 $\mu\text{g/mL}$ is still less than the threshold level. The RBCs treated with TNPs showed typical biconcave morphology, which was consistent with the results of the hemolysis analysis. All of the above can indicate that TNPs have low toxicity and the potential to be used as biomedical materials.

3.7. In vivo wound healing assay

In view of the mild photothermal properties, various enzyme activities, excellent in vitro antibacterial ability, and excellent biocompatibility of TNPs, we evaluated the in vivo antibacterial ability of TNPs (ethical code of animal experiments: IACUC-20220265). An animal wound model of *S. aureus* infection with an area of about 1.0 cm^2 was established on the back of balb/c mice. The specific process of the animal experiment is represented by the time axis (Fig. 7A). Mice were randomly divided into 6 groups: (1) control; (2) TNPs+H₂O₂/1064 nm; (3) TNPs+H₂O₂; (4) TNPs+1064 nm; (5) 1064 nm; (6) TNPs. After 1 day of infection with *S. aureus*, the mice in each group were treated accordingly. The 1064 nm laser irradiation time was 10 min, the laser power was 2.0 W/cm², the temperature of the light treatment was recorded by a thermal imaging camera, and the working concentrations of hydrogen peroxide and TNPs were 2 mM and 250 $\mu\text{g/mL}$, respectively. The wounds of mice were photographed daily.

As expected, in line with the in vitro studies, the temperature of infected skin increased (25.7 °C) compared to that of the PBS group (Figs. 7B, 7C). As can be seen from Fig. 7D, on the first day, the inflammatory response of the wounds of the mice in each group was observed, and the *S. aureus* wound model was successfully constructed. And then the mice in each group were treated accordingly. For the first 3 days, there was little change in wound size in mice treated with different treatments (Fig. 7D-7 F). But on the 4th day, the wound healing speed of the TNPs+H₂O₂/1064 nm group, TNPs+H₂O₂ group, and TNPs+1064 nm group was faster than that of the control group, which indicated that both the single antibacterial group and the synergistic antibacterial group had the better anti-infection ability. On the 8th day,

obvious pink new skin could be observed in the wounds of the TNPs+H₂O₂/1064 nm group, TNPs+H₂O₂ group, and TNPs+1064 nm group. The TNPs+H₂O₂/1064 nm group showed a tendency to heal completely, slightly better than the wounds in the TNPs+H₂O₂ group and TNPs+1064 nm group; while the control group, 1064 nm group and TNPs group were all visible wounds. In addition, fluorescence sections of tissue probed with DCFH-DA and DAPI were used to observe ROS generation in vivo in mice. Compared with the control group, green fluorescence in the TNPs+H₂O₂ group and the TNPs+H₂O₂/1064 nm group was significantly increased (Fig. S14), indicating that TNPs catalyzed H₂O₂ to generate a large amount of ROS at the infection site, which is consistent with the conclusion of the mouse wound infection model. In conclusion, the synergistic antibacterial group exhibited faster anti-infection and wound healing abilities than the single antibacterial group and the control group. Indicators of wound healing include not only reduction in the wound area, but also scabs, swelling, and scarring [47,48].

The skin tissues at mice wound sites were collected and stained with H&E and Masson's trichrome for histological analysis to evaluate the wound healing in each group. As shown in Fig. 7G, compared with the treatment group, obvious inflammatory cells were seen in the wounds of the control group, 1064 nm group, and TNPs group; in addition, only the basic structures of regenerated skin tissue, such as epithelium and dermis, granulation were observed in these groups. In the TNPs+H₂O₂/1064 nm group, the TNPs+H₂O₂ group, and the TNPs+1064 nm group, the inflammation of the wound tissue was reduced, the new epidermis increased, and the obvious hair follicle tissue structure was seen. At the same time, the corresponding Masson-stained image (Fig. 7H) showed that more tissue-structured aligned collagen (blue) was formed compared to the other groups, indicating the formation of new tissue.

Previous reports have shown that cytokine-regulated cellular activity always affects the wound healing process [49–51]. Therefore, in the mouse full-thickness skin defect model, vascular endothelial growth factor (VEGF) was selected as an indicator to evaluate the effectiveness of different treatment groups in the wound healing process. VEGF is an important factor in angiogenesis in the late stage of wound healing. From Fig. S15, the expression level of VEGF in the synergistic antibacterial group was higher than that in the single antibacterial group and the first three groups, indicating that the combination of PTT and CDT antibacterial has the effect of promoting wound healing. Further, through the histological analysis of the main tissues, the safety of TNPs treatment was observed. Fig. S16 is the H&E staining images of the heart, liver, spleen, lung, and kidney. It can be seen that no obvious pathological damage or abnormality was found after TNPs treatment.

3.8. In vivo migration assay

To evaluate the tissue penetration ability of TNPs in the presence of H₂O₂ and 1064 nm laser, we established a subcutaneous pustule model of *S. aureus* infection, and the treatment process is shown in Fig. 8A. First, the mice were injected subcutaneously with *S. aureus*, and obvious swelling of the mouse skin could be observed on the 0th day, which indicated the successful establishment of the mouse pustule model. From day 1, for the TNPs+H₂O₂/1064 nm group, 50 μL of TNPs solution (500 $\mu\text{g/mL}$) and 50 μL of H₂O₂ solution (4 mM) were injected near the mouse pustules, followed by 1064 nm light irradiation. PTT was performed, and the temperature changes of the infected site were recorded by an infrared thermal imager after different treatments (Figs. 8B, 8C). The temperature of the pure PBS and the light group rose to 31.9 °C and 35.0 °C after 10 min of 1064 nm light irradiation, which was not enough to denature bacterial proteins and enzymes. And after TNPs treatment, the local temperature at the abscess site rapidly increased to 50 °C. These results suggest that TNPs are capable of accumulating at the site of infection. As shown in Fig. 8D, on day 1 and day 2, there was no significant difference in the pustules of mice in the 6 groups. On the 3rd day, the pustules of the mice in the TNPs+H₂O₂/1064 nm group,

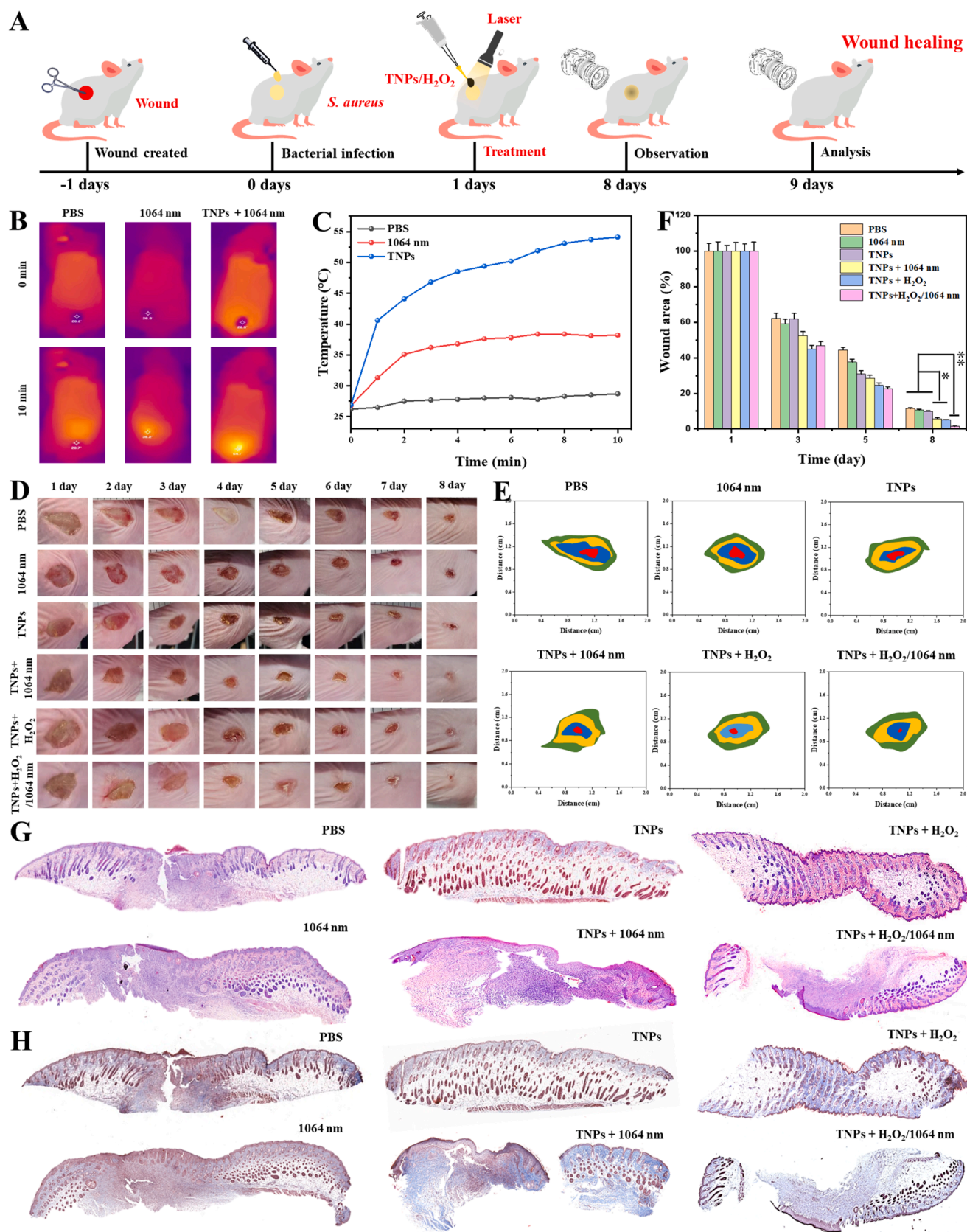


Fig. 7. *In vivo* antibacterial activity and **pustule** healing effect of TNPs in chronic wounds infected by *S. aureus*. A) Diagram of treatment of TNPs in chronic wounds caused by *S. aureus*. B) Thermographic images and C) photothermal heating curves of BALB/c chronic **pustule** mice exposed to 1064 nm at 0 and 10 min. D) Representative photographs of treated chronic wounds. E) Traces of wound-bed closure at 8 days. F) Quantitative analysis of the remaining treated wound sites separately. (* $P < 0.5$ and ** $P < 0.01$). G) Photomicrographs of tissues with H&E and H) Masson's trichrome staining of the wound tissue.

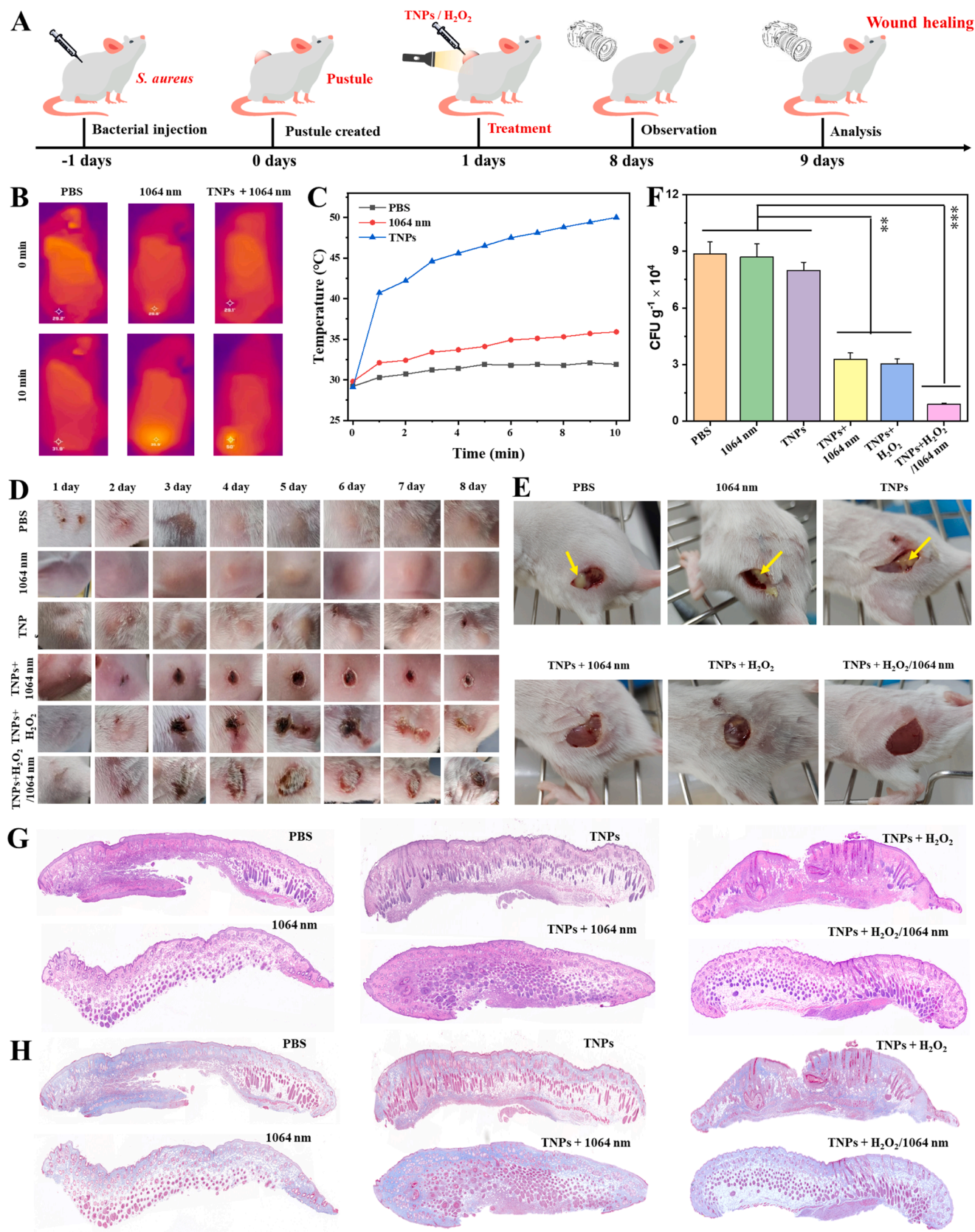


Fig. 8. *In vivo* wound healing profiles. A) Diagram of TNPs treatment in mice with chronic abscesses caused by *S. aureus*. B) Thermographic images and C) photothermal heating curves of BALB/c chronic wound mice exposed to 1064 nm at 0 and 10 min. D) Pustule images of *S. aureus*-infected abscesses after treatments. E) Images of pus after wound sampling. F) Counted from the skin tissues of *S. aureus*-infection sites in the six groups. (** $P < 0.01$ and *** $P < 0.001$). G) Photomicrographs of pustule tissues with H&E and H) Masson's trichrome staining of the pustule tissues.

TNPs+H₂O₂ group, and TNPs+ 1064 nm group were damaged, and the wounds were significantly reduced and scabbed after 8 days. Further, the skin of the mouse pustules was sampled. As shown in Fig. 8E, obvious pus exudation could be seen in the PBS group, 1064 nm group, and TNPs group after sampling; the single antibacterial group was only accompanied by a slight subcutaneous abscess; while the synergistic antibacterial group had no pus and inflammatory reaction. The in vivo antibacterial effect of TNPs was investigated using the expansion plate method (Fig. 8F). The analysis revealed that TNPs could be used for eradicating *S. aureus* in vivo.

The study of skin penetration in vivo can better reflect the potential as an efficient antibacterial nanoagent. We labeled TNPs with Cyanine 5 (Cy5) and used the mouse pustules as a model to evaluate the transdermal penetration behavior of TNPs in mouse skin by the distribution of fluorescence and penetration depth. Fig. S17 is the cross-sectional fluorescence image perpendicular to the skin surface, which clearly shows the distribution of TNPs in the skin at the pustule under different conditions. The red fluorescence of pure TNPs was mainly confined to the epidermis, while the fluorescence of the TNPs+H₂O₂ group and TNPs+H₂O₂/1064 nm group was dispersed in the whole dermis area. The results show that TNPs can penetrate dense skin and are widely distributed in the dermis under the impetus of O₂.

Next, we assessed the expression levels of HIF-1 α , an O₂-dependent transcriptional activator that is ubiquitous in the cytoplasm. When tissues are under hypoxic conditions, HIF-1 α accumulates, and translocates into the nucleus, dimerizes with HIF-1 β , and binds to the HIF-1 α binding site (HBS) to promote the transcription of various target genes. In Fig. S18, the expression of HIF-1 α in the TNPs+H₂O₂ group and TNPs+H₂O₂/1064 nm group was significantly reduced, because the O₂ generated by TNPs relieved the hypoxic environment at the pustule. Additionally, the expression of VEGF also decreased and inhibited the blood supply to the pustule, resulting in the gradual ischemic necrosis of the skin at the pustule, so the destruction of the pustule in the experimental group can be observed in Fig. 8D (day 3). The skin tissue from the pustule site of the mice was collected and histologically analyzed with H&E and Masson's trichrome staining to evaluate the pustule healing in each group. As shown in Fig. 8G, compared with the treatment group, obvious inflammatory cells were found in the wounds of the control group, 1064 nm group, and TNPs group. In the TNPs+H₂O₂/1064 nm group, TNPs+H₂O₂ group, and TNPs+ 1064 nm group, the inflammation of the wound tissue was reduced, the new epidermis increased, and the obvious hair follicle tissue structure was seen. At the same time, the corresponding Masson-stained image (Fig. 8H) showed that more tissue-structured aligned collagen (blue) was formed compared to the other groups, indicating the formation of new tissue.

Moreover, immunohistochemical staining was used to detect pro-inflammatory cytokines after different treatments. In the early stage of inflammation, TNF- α is crucial for the induction of the inflammatory response. Nevertheless, long-term high levels of TNF- α expression are damaging to the human body. As shown in Fig. S19, green fluorescence stained by TNF- α could be observed in the skin of the pustules in the PBS group, 1064 nm group, and TNPs group, indicating the widespread presence of inflammation. While the synergistic group of antibacterial agents efficiently suppressed the initial inflammatory responses. Unexpectedly, the expression of TNF- α was significantly enhanced in the TNPs+H₂O₂ group, which was attributed to the enhanced inflammatory response induced by excess ROS. Therefore, TNPs have an obvious inhibitory effect on bacteria in vivo and the ability to promote healing at the site of infection but have no obvious toxicity. So TNPs can be considered an ideal substitute in the biomedical field.

4. Conclusion

In summary, a novel NIR-II light-responsive tadpole-like TNPs with intrinsic POD-like, CAT-like, and GSHOx-like activities has been successfully produced for the healing of the bacteria-infected wound. It

produces \bullet OH at a very low concentration of hydrogen peroxide of 0.006%, which can damage bacterial cell membranes, proteins, and DNA. Moreover, the GSHOx-like activity is capable of destroying the anti-oxidative mechanism of bacteria itself, thus improving the permeability of cell membranes and greatly enhancing the killing effect of ROS. Furthermore, TNPs not only show good photothermal properties under 1064 nm laser irradiation but also achieve deep tissue penetration by O₂, thereby realizing PTT/CDT for synergistic antibacterial purposes. The synergistic therapy achieved 92.8% and 99.2% sterilization rates against *E. coli* and *S. aureus*, respectively. On the premise of good biocompatibility, TNPs also showed excellent tissue penetration ability in the mouse pustule experiment. Therefore, O₂-driven TNPs as an antibacterial nanoagent provides a promising strategy for transdermal drug delivery and antibacterial therapy.

CRediT authorship contribution statement

Yumeng Gao: Methodology, Investigation, Proof-reading and editing. **Wentao Wang:** Conceptualization, Methodology, Investigation, Writing – original draft, Visualization. **Mohsen Mohammadniaei:** Conceptualization, Methodology, Investigation, Writing – original draft. **Ming Zhang:** Conceptualization, Methodology, Investigation, Visualization. **Jian Shen:** Conceptualization, Supervision, Project administration, Funding acquisition. **Ninglin Zhou:** Conceptualization, Methodology, Proof-reading and editing.

Declaration of Competing Interest

The authors declare that they have no known competing financial interests or personal relationships that could have appeared to influence the work reported in this paper.

Data Availability

Data will be made available on request.

Acknowledgments

We are grateful for the financial support from the Key Project of the Natural Science Foundation for Jiangsu Province (Grant No. BE2020347), Jiangsu Engineering Research Center for Biomedical Function Materials, Jiangsu Collaborative Innovation Center of Biomedical Functional Materials, and Jiangsu Key Laboratory of Bio-functional Materials.

Appendix A. Supporting information

Supplementary data associated with this article can be found in the online version at doi:10.1016/j.apcatb.2022.122314.

References

- [1] G.C. Bibek, S. Sahukhal Gyan, O. Elasri Mohamed, Role of the msaABCR operon in cell wall biosynthesis, autolysis, integrity, and antibiotic resistance in *Staphylococcus aureus*, *Antimicrob. Agents Ch.* 63 (2019) e00680-00619.
- [2] S.B. Levy, B. Marshall, Antibacterial resistance worldwide: causes, challenges and responses, *Nat. Med.* 10 (2004) S122–S129.
- [3] A.K. Nanayakkara, H.W. Boucher, V.G. Fowler Jr, A. Jezek, K. Outtersson, D. E. Greenberg, Antibiotic resistance in the patient with cancer: escalating challenges and paths forward, *CA-Cancer J. Clin.* 71 (2021) 488–504.
- [4] T.A. Wencewicz, Crossroads of antibiotic resistance and biosynthesis, *J. Mol. Biol.* 431 (2019) 3370–3399.
- [5] S. Bhunia, K.A. Deo, A.K. Gaharwar, 2D covalent organic frameworks for biomedical applications, *Adv. Funct. Mater.* 30 (2020) 2002046.
- [6] G. Chedid, A. Yassin, Recent trends in covalent and metal organic frameworks for biomedical applications, *Nanomaterials* 8 (2018) 916.
- [7] H. Yazdani, M.-A. Shahbazi, R.S. Varma, 2D and 3D covalent organic frameworks: cutting-edge applications in biomedical sciences, *ACS Appl. Bio Mater.* 5 (2022) 40–58.

- [8] S. Chen, J. Lu, T. You, D. Sun, Metal-organic frameworks for improving wound healing, *Coord. Chem. Rev.* 439 (2021), 213929.
- [9] X. Han, G. Boix, M. Balcerzak, O.H. Moriones, M. Cano-Sarabia, P. Cortés, N. Bastús, V. Puentes, M. Llagostera, I. Imaz, D. Maspocho, Antibacterial films based on MOF composites that release iodine passively or upon triggering by near-infrared light, *Adv. Funct. Mater.* 32 (2022) 2112902.
- [10] W.C. Hu, M.R. Younis, Y. Zhou, C. Wang, X.-H. Xia, In situ fabrication of ultrasmall gold nanoparticles/2D MOFs hybrid as nanozyme for antibacterial therapy, *Small* 16 (2020) 2000553.
- [11] Y. Fu, J. Jiang, Q. Zhang, X. Zhan, F. Chen, Correction: robust liquid-repellent coatings based on polymer nanoparticles with excellent self-cleaning and antibacterial performances, *J. Mater. Chem. A* 5 (2017), 1313-1313.
- [12] C. Liu, Y. Guo, X. Wei, C. Wang, M. Qu, D.W. Schubert, C. Zhang, An outstanding antichlorine and antibacterial membrane with quaternary ammonium salts of alkenes via in situ polymerization for textile wastewater treatment, *Chem. Eng. J.* 384 (2020), 123306.
- [13] H. Xue, Z. Zhao, S. Chen, H. Du, R. Chen, J.L. Brash, H. Chen, Antibacterial coatings based on microgels containing quaternary ammonium ions: Modification with polymeric sugars for improved cytocompatibility, *Colloid Interface Sci. Commun.* 37 (2020), 100268.
- [14] J. Chen, J. Yang, W. Chen, Y. Wang, G. Song, H. He, H. Wang, P. Li, G.P. Wang, Tri-functional SERS nanoplateform with tunable plasmonic property for synergistic antibacterial activity and antibacterial process monitoring, *J. Colloid Interface Sci.* 608 (2022) 2266-2277.
- [15] S. Wang, B. Chen, L. Ouyang, D. Wang, J. Tan, Y. Qiao, S. Ge, J. Ruan, A. Zhuang, X. Liu, R. Jia, A novel stimuli-responsive injectable antibacterial hydrogel to achieve synergistic photothermal/gene-targeted therapy towards uveal melanoma, *Adv. Sci.* 8 (2021) 2004721.
- [16] M. Chang, Z. Hou, M. Wang, C. Yang, R. Wang, F. Li, D. Liu, T. Peng, C. Li, J. Lin, Single-atom Pd nanozyme for ferroptosis-boosted mild-temperature photothermal therapy, *Angew. Chem. Int. Ed.* 60 (2021) 12971-12979.
- [17] Y. Yang, Z. Liu, Chemiluminescent nanosystems for imaging cancer chemodynamic therapy, *Chem* 6 (2020) 2127-2129.
- [18] T. Dong, J. Jiang, H. Zhang, H. Liu, X. Zou, J. Niu, Y. Mao, M. Zhu, X. Chen, Z. Li, Y. Chen, C. Shi, X. Yang, PFP@PLGA/Cu₁₂Sb₄S₁₃-mediated PTT ablates hepatocellular carcinoma by inhibiting the RAS/MAPK/MT-CO₁ signaling pathway, *Nano Conver.* 8 (2021) 29.
- [19] X. Shan, X. Zhang, C. Wang, Z. Zhao, S. Zhang, Y. Wang, B. Sun, C. Luo, Z. He, Molecularly engineered carrier-free co-delivery nanoassembly for self-sensitized photothermal cancer therapy, *J. Nanobiotechnol.* 19 (2021) 282.
- [20] Y. Wang, H. Yao, Y. Zu, W. Yin, Biodegradable MoO₃@MB incorporated hydrogel as light-activated dressing for rapid and safe bacteria eradication and wound healing, *RSC Adv.* 12 (2022) 8862-8877.
- [21] J. Li, W. Zhang, W. Ji, J. Wang, N. Wang, W. Wu, Q. Wu, X. Hou, W. Hu, L. Li, Near infrared photothermal conversion materials: mechanism, preparation, and photothermal cancer therapy applications, *J. Mater. Chem. B* 9 (2021) 7909-7926.
- [22] Y. Han, B. Qu, J. Li, X. Zhang, X. Peng, W. Li, R. Zhang, A simple POM clusters for in vivo NIR-II photoacoustic imaging-guided NIR-II photothermal therapy, *J. Inorg. Biochem.* 209 (2020), 111121.
- [23] D. Li, B. Chen, W.J. Wu, Z.X. Ying, Influence of laser wavelength on the thermal responses of port wine stain lesions in light, moderate and heavy pigmented skin, *Appl. Therm. Eng.* 117 (2017) 193-203.
- [24] C. Zhao, X. Jian, X. Zhang, J. Guo, Z. Gao, Y.-Y. Song, Rapid capture and photocatalytic inactivation of target cells from whole blood by rotating janus nanotubes, *ACS Appl. Mater. Interfaces* 13 (2021) 12972-12981.
- [25] A. Elbourne, S. Cheeseman, P. Atkin, N.P. Truong, N. Syed, A. Zavabeti, M. Mohiuddin, D. Esrafilzadeh, D. Cozzolino, C.F. McConville, M.D. Dickey, R. J. Crawford, K. Kalantar-Zadeh, J. Chapman, T. Daeneke, V.K. Truong, Antibacterial liquid metals: biofilm treatment via magnetic activation, *ACS Nano* 14 (2020) 802-817.
- [26] Y. Zhang, Y. Pi, Y. Hua, J. Xie, C. Wang, K. Guo, Z. Zhao, Y. Yong, Bacteria responsive polyoxometalates nanocluster strategy to regulate biofilm microenvironments for enhanced synergistic antibiofilm activity and wound healing, *Theranostics* 10 (2020) 10031-10045.
- [27] D. Hu, Y. Deng, F. Jia, Q. Jin, J. Ji, Surface charge switchable supramolecular nanocarriers for nitric oxide synergistic photodynamic eradication of biofilms, *ACS Nano* 14 (2020) 347-359.
- [28] D. Hu, L. Zou, W. Yu, F. Jia, H. Han, K. Yao, Q. Jin, J. Ji, Relief of biofilm hypoxia using an oxygen nanocarrier: a new paradigm for enhanced antibiotic therapy, *Adv. Sci.* 7 (2020) 2000398.
- [29] Y. Chen, Q. Ji, G. Zhang, H. Liu, J. Qu, Synergetic lipid extraction with oxidative damage amplifies cell-membrane-destructive stresses and enables rapid sterilization, *Angew. Chem. Int. Ed.* 60 (2021) 7744-7751.
- [30] H. Wang, K. Wang, L. He, Y. Liu, H. Dong, Y. Li, Engineering antigen as photosensitizer nanocarrier to facilitate ROS triggered immune cascade for photodynamic immunotherapy, *Biomaterials* 244 (2020), 119964.
- [31] M. Kiristi, V.V. Singh, B. Esteban-Fernández de Ávila, M. Uygün, F. Soto, D. Aktaş Uygün, J. Wang, Lysozyme-based antibacterial nanomotors, *ACS Nano* 9 (2015) 9252-9259.
- [32] J. Peng, S. Xie, K. Huang, P. Ran, J. Wei, Z. Zhang, X. Li, Nitric oxide-propelled nanomotors for bacterial biofilm elimination and endotoxin removal to treat infected burn wounds, *J. Mater. Chem. B* 10 (2022) 4189-4202.
- [33] M. Chang, M. Wang, M. Wang, M. Shu, B. Ding, C. Li, M. Pang, S. Cui, Z. Hou, J. Lin, A multifunctional cascade bioreactor based on hollow-structured Cu₂MoS₄ for synergistic cancer chemo-dynamic therapy/starvation therapy/phototherapy/immunotherapy with remarkably enhanced efficacy, *Adv. Mater.* 31 (2019) 1905271.
- [34] J. Shan, K. Yang, W. Xiu, Q. Qiu, S. Dai, L. Yuwen, L. Weng, Z. Teng, L. Wang, Cu₂MoS₄ nanozyme with NIR-II light enhanced catalytic activity for efficient eradication of multidrug-resistant bacteria, *Small* 16 (2020) 2001099.
- [35] S.-Y. Yin, G. Song, Y. Yang, Y. Zhao, P. Wang, L.-M. Zhu, X. Yin, X.-B. Zhang, Persistent regulation of tumor microenvironment via circulating catalysis of MnFe₂O₄@Metal-organic frameworks for enhanced photodynamic therapy, *Adv. Funct. Mater.* 29 (2019) 1901417.
- [36] B.-B. Chen, D.-K. Ma, Q.-P. Ke, W. Chen, S.-M. Huang, Indented Cu₂MoS₄ nanosheets with enhanced electrocatalytic and photocatalytic activities realized through edge engineering, *Phys. Chem. Chem. Phys.* 18 (2016) 6713-6721.
- [37] H. Chen, K. Zhang, W. Chen, I. Ali, P. Wu, D. Liu, L. Song, Raman scattering of single crystal Cu₂MoS₄ nanosheet, *AIP Adv.* 5 (2015), 037141.
- [38] N. Ma, B. Wei, W. Cao, H. Gao, L. Xu, Carbon dots/ Cu₂MoS₄ nanosheets hybrids with efficient photoelectrochemical performance, *Mater. Lett.* 197 (2017) 79-82.
- [39] K. Zhang, W. Chen, Y. Lin, H. Chen, Y.A. Haleem, C. Wu, F. Ye, T. Wang, L. Song, Self-assembly of ultrathin Cu₂MoS₄ nanobelts for highly efficient visible light-driven degradation of methyl orange, *Nanoscale* 7 (2015) 17998-18003.
- [40] Z. Liu, T. Li, N. Li, Y. Wang, L. Chen, X. Tang, M. Wan, C. Mao, GSH-induced chemotaxis nanomotors for cancer treatment by ferroptosis strategy, *Sci. China Chem.* 65 (2022) 989-1002.
- [41] M. Wan, Z. Liu, T. Li, H. Chen, Q. Wang, T. Chen, Y. Tao, C. Mao, Zwitterion-based hydrogen sulfide nanomotors induce multiple acidosis in tumor cells by destroying tumor metabolic symbiosis, *Angew. Chem. Int. Ed.* 60 (2021) 16139-16148.
- [42] W. Yu, R. Lin, X. He, X. Yang, H. Zhang, C. Hu, R. Liu, Y. Huang, Y. Qin, H. Gao, Self-propelled nanomotor reconstructs tumor microenvironment through synergistic hypoxia alleviation and glycolysis inhibition for promoted anti-metastasis, *Acta Pharm. Sin.* B 11 (2021) 2924-2936.
- [43] C. Zhao, X. Jian, Z. Gao, Y.-Y. Song, Plasmon-mediated peroxidase-like activity on an asymmetric nanotube architecture for rapid visual detection of bacteria, *Anal. Chem.* 94 (2022) 14038-14046.
- [44] X. Meng, D. Li, L. Chen, H. He, Q. Wang, C. Hong, J. He, X. Gao, Y. Yang, B. Jiang, G. Nie, X. Yan, L. Gao, K. Fan, High-performance self-cascade pyrite nanozymes for apoptosis-ferroptosis synergistic tumor therapy, *ACS Nano* 15 (2021) 5735-5751.
- [45] B. Sun, Z. Ye, M. Zhang, Q. Song, X. Chu, S. Gao, Q. Zhang, C. Jiang, N. Zhou, C. Yao, J. Shen, Light-activated biodegradable covalent organic framework-integrated heterojunction for photodynamic, photothermal, and gaseous therapy of chronic wound infection, *ACS Appl. Mater. Interfaces* 13 (2021) 42396-42410.
- [46] X. Jian, J. Guo, J. Xu, Z. Yang, Y. Shu, Z. Gao, Y.-Y. Song, Mineralization of dandelion as an enzyme-like nanoelectrode for ultrasensitive monitoring of H₂O₂ at a single-cell level, *ACS Sustain. Chem. Eng.* 10 (2022) 11367-11375.
- [47] X. Chu, F. Wu, B. Sun, M. Zhang, S. Song, P. Zhang, Y. Wang, Q. Zhang, N. Zhou, J. Shen, Genipin cross-linked carbon dots for antimicrobial, bioimaging and bacterial discrimination, *Colloids Surf., B* 190 (2020), 110930.
- [48] G. Zhao, P.C. Hochwalt, M.L. Usui, R.A. Underwood, P.K. Singh, G.A. James, P. S. Stewart, P. Fleckman, J.E. Olerud, Delayed wound healing in diabetic (db/db) mice with *Pseudomonas aeruginosa* biofilm challenge: a model for the study of chronic wounds, *Wound Repair Regen.* 18 (2010) 467-477.
- [49] V. Bansal, D. Hoppensteadt, E. Litinas, I. Thethi, J. Fareed, Differential modulation of cytokines by VEGF in end stage renal disease, *Blood* 116 (2010), 5187-5187.
- [50] M. Hou, Y. Wei, Z. Zhao, W. Han, R. Zhou, Y. Zhou, Y. Zheng, L. Yin, Immuno-engineered nanodecoys for the multi-target anti-inflammatory treatment of autoimmune diseases, *Adv. Mater.* 34 (2022) 2108817.
- [51] A. Novikov, E. Aleksandrova, Z. Verizhnikova, T. Panafidina, T. Popkova, D. Karateev, E. Luchihina, E. Nasonov, AB0030 cytokine profiles in systemic lupus erythematosus and rheumatoid arthritis, *Ann. Rheum. Dis.* 75 (2016) 907.